Monthly Notices
of the
ROYAL ASTRONOMICAL SOCIETY

MNRAS **492,** 589–602 (2020) doi:10.1093/mnras/stz3407
Advance Access publication 2019 December 5

Asteroid masses obtained with INPOP planetary ephemerides

A. Fienga,[1,2★] C. Avdellidou[3] and J. Hanuš[4]

[1]*Geoazur, CNRS, Observatoire de la Côte d'Azur, Université Côte d'Azur, 250 av. A. Einstein, F-06560 Valbonne, France*
[2]*IMCCE, CNRS, Observatoire de Paris, Université PSL, 77 av. Denfert-Rochereau, F-75014 Paris, France*
[3]*Lagrange, CNRS, Observatoire de la Côte d'Azur, Université Côte d'Azur, CS 34229, F-06304, Nice Cedex 4, France*
[4]*Institute of Astronomy, Charles University, Prague, V Holešovičkách 2, CZ-18000, Prague 8, Czech Republic*

Accepted 2019 November 22. Received 2019 November 22; in original form 2019 September 22

ABSTRACT

In this paper, we present masses of 103 asteroids deduced from their perturbations on the orbits of the inner planets, in particular Mars and the Earth. These determinations and the INPOP19a planetary ephemerides are improved by the recent Mars orbiter navigation data and the updated orbit of Jupiter based on the Juno mission data. More realistic mass estimates are computed by a new method based on random Monte Carlo sampling that uses up-to-date knowledge of asteroid bulk densities. We provide masses with uncertainties better than 33 per cent for 103 asteroids. Deduced bulk densities are consistent with those observed within the main spectroscopic complexes.

Key words: celestial mechanics – ephemerides – minor planets, asteroids: general.

1 INTRODUCTION

The last decade witnessed an impressive growth in the determination of physical properties of asteroids. Sizes have been massively provided by space missions, such as NASA's *WISE*/NEOWISE and JAXA's AKARI satellites, for more than 130 000 asteroids (Masiero et al. 2011, 2012, 2014; Usui et al. 2011; Alí-Lagoa et al. 2018); see also the review by Mainzer, Usui & Trilling (2015).

Dedicated spectroscopic observations (DeMeo et al. 2009) and spectrophotometry from large surveys in the visible (Carvano et al. 2010; DeMeo & Carry 2013; Binzel et al. 2019) and infrared light (Popescu et al. 2018) provided invaluable information about the asteroids surface composition, distribution of spectral classes and allowed in some cases to establish links between asteroids and meteorite types (see Section 2.3).

Density and inner structure of asteroids, which are one of the most fundamental properties, are still not well explored. These physical characteristics provide us information about the formation conditions and the evolution mechanisms, including collisions, of the early Solar system. Some attempts were made to use meteorite densities as indicators of asteroid interiors (Consolmagno, Britt & Macke 2008).

On the other hand, the determination of the average density of an asteroid requires knowledge of its mass and volume. There are different methods to determine the mass of an asteroid: (i) asteroid–spacecraft perturbations, (ii) asteroid–asteroid perturbations, (iii) observations of the motion of asteroid satellites, (iv) Yarkovsky effect, and (v) asteroid–planet perturbations.

★ E-mail: fienga@geoazur.unice.fr

The first method is by far the most accurate, but is limited to the rare instances of a close spacecraft encounter. Space missions, such as NASA's Galileo, Dawn, NEAR-Shoemaker, ESA's ROSETTA and JAXA's Hayabusa, have obtained data to derive masses for the asteroids (1) Ceres (Russell et al. 2016), (4) Vesta (Russell et al. 2012), (21) Lutetia (Pätzold et al. 2011), (25143) Itokawa (Abe et al. 2006; Fujiwara et al. 2006), (243) Ida (Belton et al. 1995), (253) Mathilde (Yeomans et al. 1997), and (433) Eros (Yeomans et al. 2000). The measurements of NASA's OSIRIS-REx and JAXA's Hayabusa2 missions also provided very accurate mass and density determinations for the near-Earth asteroids (101955) Bennu (Barnouin et al. 2019; Scheeres et al. 2019) and (162173) Ryugu (Watanabe et al. 2019).

The second method, tracking the motions of asteroids that gravitationally interact with one another, requires modelling the orbits of multiple asteroids over long periods of time and high accuracy astrometry. The best data are for the largest asteroids such as (1) Ceres, (2) Pallas, (4) Vesta, or (10) Hygeia (see Siltala & Granvik 2017; Siltala & Granvik 2019, and references therein). These authors also used Markov-chain Monte Carlo method to estimate the masses of (7) Iris, (13) Egeria, (15) Eunomia, (19) Fortuna, (29) Amphitrite, (52) Europa, and (704) Interamnia from asteroid-to-asteroid perturbations. It is expected that the high-precision astrometric observations of ESA's space mission *Gaia* (Gaia Collaboration et al. 2018) will enable us to derive the masses of about one hundred asteroids (Mouret, Hestroffer & Mignard 2007, 2008).

Using the third method, masses of some asteroids have been derived from astrometric observations of their natural satellites and the application of Kepler's third law. These resulted in mass determination for (22) Kalliope (Descamps et al. 2008; Marchis et al. 2008b), (41) Daphne (Carry et al. 2019), (45) Eugenia (Marchis et al. 2008b), (87) Sylvia (Marchis et al. 2005a; Fang, Margot & Rojo 2012), (90) Antiope (Descamps et al. 2007), (107) Camilla (Marchis et al. 2008b), (121) Hermione (Marchis et al. 2005b), (130) Elektra (Marchis et al. 2008a; Yang et al. 2016), (216) Kleopatra (Descamps et al. 2011), (283) Emma (Marchis et al. 2008a), (702) Alauda (Rojo & Margot 2011), and (762) Pulcova (Marchis et al. 2008b).

The fourth method relies on measuring the semimajor axis (a) drift ($\mathrm{d}a/\mathrm{d}t$) of an asteroid due to the non-gravitational acceleration caused by the Yarkovsky thermal effect (Bottke et al. 2006; Vokrouhlický et al. 2015) and interpret this value in terms of the physical properties of the asteroid, including its bulk density. So far, this method has been used only for small near-Earth asteroids and resulted in the measurements of the bulk density of (6489) Golevka (Chesley et al. 2003), (101955) Bennu (Chesley et al. 2014), (29075) 1950 DA (Rozitis, MacLennan & Emery 2014), (1620) Geographos (Rozitis & Green 2014), and (3200) Phaethon (Hanuš et al. 2018).

The fifth method is based on the measurements of the perturbations that mostly Main Belt asteroids produce on the orbits of the inner planets, in particular on Mars. By integrating the motion of all planets, including outer planets and the Earth–Moon system, Main Belt asteroid perturbations are included, monitored, and compared to the accurate distance measurements of the planets, which are deduced from space missions, specifically Mars orbiters. This method was used for the first time by Standish & Hellings (1989), who determined the masses of (1) Ceres, (2) Pallas, and (4) Vesta from their perturbations on Mars, making use of radio science tracking data from the Viking lander.

With the increase of the number of missions for the exploration of Mars, the computation of its orbit became more and more accurate. The INPOP (Intégrateur Numérique Planétaire de l'Observatoire de Paris) planetary ephemerides (Viswanathan et al. 2017) are particularly suited to this type of study. They have been developed since 2003 and eight previous releases have been publicly available on the INPOP website (www.imcce.fr/inpop). INPOP is based on the numerical integration of the motion of the eight planets, Pluto, Moon, and asteroids. The positions of these bodies are determined from a combination of ground- and spacecraft-based observations (Fienga et al. 2014; Viswanathan et al. 2017). The analysis of spacecraft navigation and radio science data is crucial for the construction of such ephemerides, constituting more than 65 per cent of INPOP planetary data sets used for their fits.

The centimetre accuracy and the 10-yr time span covered by the Mars orbiter data required indeed a more and more accurate description of Mars' motion. To do so, an increasing number of small bodies have been taken into account to introduce perturbations on the martian ephemerides (from five with DE405 and INPOP06 in 1998 Fienga et al. 2009, to 343 with DE430 and this work). Different strategies have been considered such as individual point-mass objects and a ring for averaging the effects of small objects (Kuchynka et al. 2010) or only individual objects (several hundreds like for DE430). At the end, each of these ephemerides obtains very accurate estimations for the planetary orbits and reduced post-fit residuals. As a by-product, asteroid masses by hundreds (343 for DE430 and following versions and about 150 for INPOP up to this work) are constrained during such fit.

However, as it was explained in Kuchynka & Folkner (2013), only a limited number of masses (23) can be trusted when computing average densities, or for comparisons with the typical densities for each asteroid type. This can be explained by two sources of uncertainties and systematic errors: one is the selection of the asteroids to be considered in the construction of the ephemeris. Indeed, different methods can be proposed for identifying asteroids that induce large enough perturbations for accurate mass determinations. Williams (1984) had proposed an analytical approach, whereas, for example, Somenzi et al. (2010) investigated selection bias based on the perturbation efficiency limited over a small, but very accurate data arc. The second source of errors comes from the difficulty of estimating systematic errors during the fit. Kuchynka & Folkner (2013) selected 3 714 asteroids in order to generate the first population of objects perturbing the planetary orbits. They estimated the masses for 343 selected asteroids taking into account systematic errors induced by the omitted asteroids (3 371 objects) using a Tikhonov regularization. This method demonstrates that, in this context, only 27 asteroids can have reliable estimations (uncertainties smaller than 33 per cent) over a selection of 343 fitted masses.

The idea of this work is not to reconsider the selection of the asteroid masses made by Kuchynka & Folkner (2013), but to use the knowledge of the physical properties of asteroids deduced from spatial or ground-based surveys to reduce the errors, enlarge the set of estimated masses, and to study their consistency with the spectral classes of the asteroids.

Section 2 introduces the INPOP dynamical modelling and gives a description of the method used for constraining asteroid masses by considering up-to-date spectral information. In Section 3, we provide our determinations of asteroid masses based on Monte Carlo estimations and discuss the possible sources of uncertainties. Finally, in Section 4 we discuss these masses in the context of previous estimations and implications for the physical properties of asteroid families.

2 METHODS

2.1 The INPOP19a planetary ephemerides and the adjustment method

Since Fienga et al. (2008), the INPOP planetary ephemerides are regularly produced and used as a scientific tool for testing alternative theories of gravity, studying variations of the solar plasma density, and estimating asteroid masses (Fienga et al. 2009, 2011, 2016). The INPOP ephemerides of not only the eight planets of our Solar system but also of Pluto and the Moon are obtained by numerically integrating the barycentric Einstein–Infeld–Hoffmann equations of motion (Moyer 1971) in a suitable relativistic time-scale and taking into account the gravitational perturbations of up to several hundreds of asteroids of the Main Belt.

In 2017, we released the latest INPOP ephemerides, INPOP17a (Viswanathan et al. 2017), built over a sample of historical and modern planetary observations from the first photographic plates of Pluto to 10 yr of Cassini radio-science experiment around Saturn and its system. Important updates concerning the model of the Moon libration explained in Viswanathan et al. (2018) are the main characteristics of INPOP17a.

Since INPOP17a, we have updated the Mars observational data by adding the latest delivery of ESA's Mars Express (MEX) observations up to 2017 in addition to the NASA Mars Global Surveyor (MGS), Mars orbiter (MO), and Mars Reconnaissance Orbiter (MRO) observations available from 1999 to 2014. We have also included the first six perijove passes of NASA's Juno mission, which orbits Jupiter on a highly eccentric orbit since 2016. These data were collected during the closest approaches of Juno to Jupiter during the first six fly-bys, from 2016 to 2018, and have

Table 1. INPOP19a data samples used for its fits. Columns 1 and 2 give the observed planet and an information on the space mission providing the observations. Columns 3 and 4 give the number of observations and the time interval, while the last column gives a priori uncertainties provided by space agencies or the corresponding navigation teams.

Planet	Type	#	Period	Averaged accuracy
Mercury	Range (m)	462	1971.29 : 1997.60	900
Mercury Messenger	Range (m)	1096	2011.23 : 2014.26	5
Mercury Mariner	Range (m)	2	1974.24 : 1976.21	100
Venus	VLBI (mas)	68	1990.70 : 2013.14	2.0
Venus	Range (m)	489	1965.96 : 1990.07	1400
Venus Vex	Range (m)	24783	2006.32 : 2011.45	7.0
Mars	VLBI (mas)	194	1989.13 : 2013.86	0.3
Mars Mex	Range (m)	30669	2005.17 : 2017.37	2.0
Mars MGS	Range (m)	2459	1999.31 : 2006.70	2.9
Mars Ody	Range (m)	20985	2002.14 : 2014.00	1.1
Mars Path	Range (m)	90	1997.51 : 1997.73	15.0
Jupiter	VLBI (mas)	24	1996.54 : 1997.94	11
Jupiter	ra/de (arcsec)	6416	1924.34 : 2008.49	0.3
Jupiter fly-bys	ra/de (mas)	5	1974.92 : 2001.00	4.0/12.0
Jupiter fly-bys	Range (m)	5	1974.92 : 2001.00	2000
Jupiter Juno	Range (m)	6	2016.65 : 2017.96	10
Saturn	ra/de (arcsec)	7826	1924.22 : 2008.34	0.3/0.3
Saturn VLBI Cass	ra/de (mas)	10	2004.69 : 2009.31	0.6/0.3
Saturn Cassini	Range (m)	165	2004.41 : 2014.38	25.0
Uranus	ra/de (arcsec)	12893	1924.62 : 2011.74	0.2/0.2
Uranus fly-bys	ra/de (mas)	1	1986.07 : 1986.07	50/50
Uranus fly-bys	Range (m)	1	1986.07 : 1986.07	2
Neptune	ra/de (arcsec)	5254	1924.04 : 2007.88	0.2/0.3
Neptune fly-bys	ra/de (mas)	1	1989.65 : 1989.65	15.0
Neptune fly-bys	Range (m)	1	1989.65 : 1989.65	10

an accuracy on Juno's orbit of less than 10 m (Durante & Iess, private communication). Improvements in the Mars residuals have also reduced the 1σ dispersion to less than 1 m for MRO/MO (compared to 1.3 m with INPOP17a) and to about 1.5 m for MEX. For MEX, the improvement between INPOP19a and INPOP17a comes from the correction of a systematic bias visible in INPOP17a residuals but less present in INPOP19a residuals. An additional correction for the solar plasma delay has been added. Finally, we implemented also the spectral constraints described in Section 2.2 in terms of asteroid modelling. In Tables 1 and 2, we show the average accuracy and the differences of the root mean squares of the MRO/MO and MEX residuals. With INPOP17a, only 150 asteroids have their masses estimated in the fit when now 345 asteroid masses are fitted as discussed in Section 3. The MRO/MO differences between INPOP17a and INPOP19a come from an improvement in the solar plasma correction during and after the conjunction period. For INPOP19a, the formulation given by Tyler et al. (1977) was applied to the full interval of time leading to less noisy residuals. The level of noise for the MEX residuals is less reduced and reaches the expected instrumental accuracy (Fienga et al. 2009).

In Table 1, we present the different data samples used for the construction of INPOP19a, including the time span and a priori uncertainties for each type of observation.

2.2 Fit with bounded value least squares

For the mass determination, we use a constrained least-squares method based on the NNLS (non-negative least squares) algorithm from Lawson & Hanson (1974), which limits the fitted parameters to be positive. A bound constrained least-squares problem consists

Table 2. Root mean squares of one-way residuals obtained with different ephemerides given in meters. For INPOP17a, the residuals are computed on the fitting interval, before 2016.1.

	MEX One-way (m)	MRO/MO one-way (m)
INPOP17a	1.55	1.26
INPOP19a	1.47	0.81

in finding x such that

$$\min \|Ax - b\|_2^2 \text{ with } \alpha < x < \delta, \tag{1}$$

where $x, \alpha, \beta \in R^m$, $A \in R^{m,n}$, and $b \in R^n$. $\| \|_2$ stands for the norm 2. Most methods for solutions of bound-constrained least-squares problems of the form of equation (1) can be categorized as active-set or interior point methods. For this work, we used an active-set method for which a sequence of equality constrained problems are solved with efficient solution methods. In particular, equation (1) is equivalent to quadratic programming problem such as finding x is equivalent as x being the

$$\min(\frac{1}{2}x^T(A^TA)x - (A^Ty)^Tx). \tag{2}$$

More specifically, we used the bounded values least squares (BVLS) algorithm by Lawson & Hanson (1995). This algorithm relies on the gradient of equation (1) with

$$w = A^T(b - Ax). \tag{3}$$

Table 3. Comparison of the derived masses from Case E to the literature values measured in binary systems or spacecraft encounters. Values with uncertainties smaller than 30 per cent of the fitted masses are kept for sake of comparisons.

Asteroid	Mass $\pm\sigma_m$ ($\times\,10^{18}$ kg)	Ref.	Mass Case E $\pm\sigma_m$ ($\times\,10^{18}$ kg)
1	939.3 $\pm$ 5	Russell et al. (2016)	938.64 $\pm$ 2.6
4	259.0 $\pm$ 0.001	Russell et al. (2012)	259.12 $\pm$ 0.7
21	1.7 $\pm$ 0.0017	Pätzold et al. (2011)	1.69 $\pm$ 0.66
22	8.1 $\pm$ 0.2	Marchis et al. (2008b)	6.40 $\pm$ 2.10
45	5.69 $\pm$ 0.12	Marchis et al. (2008b)	7.01 $\pm$ 1.90
87	14.78 $\pm$ 0.06	Marchis et al. (2005b)	18.5 $\pm$ 3.78
90	0.828 $\pm$ 0.022	Descamps et al. (2007)	0.99 $\pm$ 0.48
107	11.2 $\pm$ 0.3	Marchis et al. (2008b)	10.98 $\pm$ 3.51
121	5.381 $\pm$ 0.3	Marchis et al. (2005a)	5.37 $\pm$ 2.00
130	6.6 $\pm$ 0.4	Marchis et al. (2008a)	6.66 $\pm$ 2.20
216	4.64 $\pm$ 0.02	Descamps et al. (2011)	4.65 $\pm$ 1.19
283	1.38 $\pm$ 0.03	Marchis et al. (2008a)	2.11 $\pm$ 0.99
702	6.057 $\pm$ 0.36	Rojo & Margot (2011)	7.35 $\pm$ 2.78
762	1.4 $\pm$ 0.1	Marchis et al. (2008b)	1.47 $\pm$ 0.66

Table 4. Prior distributions of densities per spectroscopic complex for the different cases considered in the text. Unit is g cm^{-3}.

	A	B	C	D
C-complex	1.5 $\pm$ 1.0	1.8 $\pm$ 1.0	1.2 $\pm$ 1.0	2.0 $\pm$ 1.0
S-complex	3.0 $\pm$ 0.8	3.0 $\pm$ 0.8	3.0 $\pm$ 0.8	3.0 $\pm$ 0.8
X-complex	3.4 $\pm$ 1.4	3.4 $\pm$ 1.4	3.4 $\pm$ 1.4	3.4 $\pm$ 1.4
Number of runs	1900	600	600	600

Depending on the sign of each component of w, the estimated variables are ranked according to the given bounds and to the distances between the out-of-bounds (Stark & Parker 1995). The algorithm stops when all variables are strictly between their lower and upper bounds. If these conditions are not realized, an iterative procedure takes place in minimizing the difference:

$$\|A'z - b'\|_2^2, \tag{4}$$

where $A^{'}$, the matrix composed of those columns of A corresponding to variables inside the bounds and $b^{'} = b - \sum_k A_{jk} xj$, k being the index of out-of-bounds variables. A detailed description of the algorithm can be found in Lawson & Hanson (1974) and Stark & Parker (1995).

For this work, bounds have been selected according to the parameters of the fit: For asteroid masses, the lower bounds and the upper bounds are chosen according to the a priori masses and the a priori uncertainties deduced from the literature (see Section 2.3). For parameters other than the asteroid masses such as initial conditions of planetary orbits, the mass of the Sun or the Sun oblateness, very large bounds (equivalent to infinite bounds) are used. These extremely large bounds are equivalent to a fit with no bounds for these parameters (Stark & Parker 1995).

2.3 Selection of a priori values

The selection of 343 asteroids perturbing the planetary orbits is done based on the method of Kuchynka & Folkner (2013) and Folkner et al. (2014). This selection was obtained by considering the amplitudes and the frequencies of the asteroid perturbations as described by Williams (1984) or Kuchynka (2010). Kuchynka & Folkner (2013) has confirmed this selection by adding a Tikhonov regularization in order to estimate the systematic error induced by an imperfect selection of asteroid in the dynamical modelling of the planetary orbits. It was then demonstrated that neglecting objects not included in the 343 main list introduce only negligible systematics. For these reasons, we keep this list of 343 main perturbers for the present study. As in Folkner et al. (2014), *a priori* constraints were used in the fit for the same selection of asteroids.

For the estimation of the a priori mass values and uncertainties, two cases are considered: (i) asteroid masses directly measured by other methods than planetary ephemerides, mainly binary systems or spacecraft (s/c) fly-bys, and (ii) masses that can be deduced by indirect means (using diameters and spectroscopic classes and assuming averaged density classes).

If a mass was directly estimated thanks to s/c fly-bys or because the asteroid has a satellite, the measured mass is taken as the first guess for the integration and the 3σ uncertainty is taken as a priori uncertainties. As indicated in Table 3, only 14 objects among our list of 343 belong to this category.

If the mass was not directly measured, INPOP used, as first guess, a mass deduced from the measured asteroid diameter (D) and an assumed density ($\rho_{\rm guess}$). A first selection of diameters was extracted by using radiometric measurements from the *WISE* or AKARI catalogues (273 objects, whose references are given in the supplementary material, Table A1). A second selection of diameters was deduced from stellar occultations or disc-resolved observations by ground-based telescopes equipped with adaptive optics systems (64 objects; see Table A1).

Concerning the density, we separated the sample into three taxonomic complexes C, S, and X according to the spectral information extracted from the MP3C data base (mp3c.oca.eu). Priority was given to Bus-DeMeo taxonomy (DeMeo et al. 2009). If not available, we used Tholen (1989) or Bus & Binzel (2002). Each complex is separated into classes. The C-complex includes asteroids displaying reflectance spectra with weak or no features and with flat or very moderate slopes. The C-complex asteroids are associated with carbonaceous chondrite meteorites. The S-complex includes asteroids with absorption bands typical of ordinary chondrite meteorites, indicating a silicate composition. The X-complex is characterized by moderately sloped spectra with no or weak features. It is compositionally degenerate, as it contains objects with high and low albedos that could have different compositions. In the case when an asteroid is classified only in Tholen taxonomy as P-type, we included it in the C-complex population for the runs described below. This is because the P-types have by definition low albedo value similar to the C-complex asteroids and previous works suggest low-density values for them.

As described in Section 2.2, the BVLS method requires to provide the estimations of minimum and maximum values constraining the interval of possible values for the fitted parameters. In order to obtain consistent masses, it is reasonable to provide to the fit bounds that use our existing knowledge of asteroid sizes and densities. Considering the density contribution, one possible method is to use for lower and upper density bounds the $\pm 1\sigma$ standard deviation obtained when compiling spectral observations. We provide these values in Table 4. In order to obtain the standard deviation of the density, we used as input the compilation of densities of Carry (2012). From this list of asteroids, we filtered out those that are marked with a cross (meaning macroporosity larger than 100 per cent), as well as the densities that have uncertainties greater than 30 per cent. Next, we separated the remaining sample following

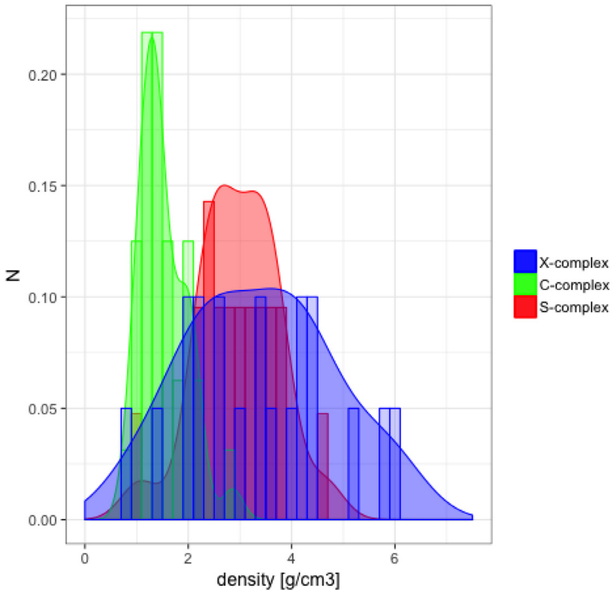

Figure 1. Distribution of densities per complex types as obtained by filtering Carry (2012).

the spectroscopic complexes S, C, and X. Moreover, we removed from the C-complex asteroids with unrealistic densities (e.g. 4–8 g cm^{-3}). Fig. 1 shows the distribution of the densities kept for the analysis.

This resulted in each asteroid having fixed upper and lower bounds depending on its taxonomic type. In doing so, the fitted masses may depend on the fixed bound selection. This is the reason why a more general approach is considered. For each asteroid, a Gaussian distribution for its lower and upper bounds is implemented and random selections of values for the lower and upper bounds is done from these Gaussian distributions. They are centred on the minimum (resp. maximum) value acceptable according to the density distribution given in Table 4, with a dispersion of $\sigma_p/2$, guaranteeing that 100 per cent of the lower (respectively upper) constraint are smaller (respectively greater) than the average density for the corresponding complex. For each run, a Monte Carlo sampling is done for selecting randomly a value from the lower and upper bound Gaussian distributions. In using random selection of the bounds, we tested the sensitivity of the method to the selection of the bounds. The bounds are not fixed but vary from one run to another.

Furthermore, because of the uncertainties in the spectral classifications and to avoid too strong constraints in the fit, we consider also different possible distributions of densities following four cases (A, B, C, and D) given in Table 4. For the C-complex that represents 63 per cent of the total sample, we tested several additional sizes of Gaussian distributions compared to the reference Case A, with density slightly greater (Cases B and D) or lower (Case C).

We then translated the density bounds into mass bounds as $\frac{4}{3}\pi D^3 \rho_{\text{guess}}$, i.e. assuming that the quoted D-values are spherical equivalent diameters. A priori uncertainties on the initial guess values for the masses were deduced by including the 3σ diameter uncertainties to the density lower and upper bounds. We use 3σ diameter uncertainties for safety against biasing our final results: it is known that the typical thermal modeling uncertainty on the diameter is of the order of 10–15 per cent relative value (Harris & Lagerros 2002; Harris 2006) and that the quoted uncertainties from the WISE and AKARI catalogues could be slightly underestimated (Hanuš et al. 2015). Therefore, we assume a relative uncertainty of 15 per cent on each diameter as 1σ.

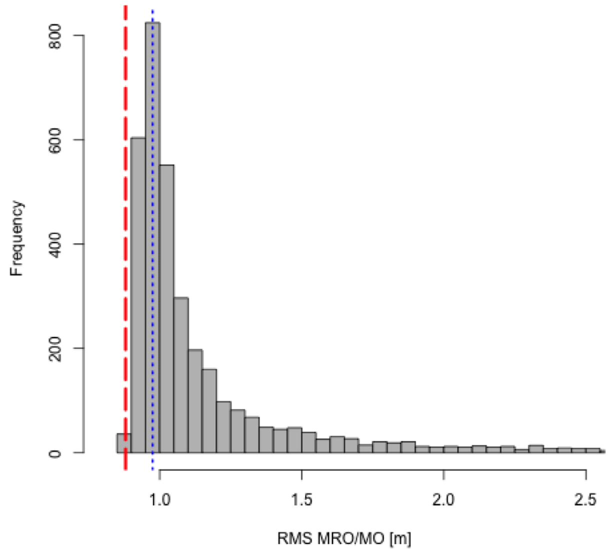

Figure 2. Distribution of the MRO/MO root mean square (rms) for the 3600 Monte Carlo runs. The dot line indicates the INPOP17a rms, whereas the dashed line gives the INPOP19a RMS.

Once the bounds are estimated, regular BVLS fit is made leading to post-fit residuals and mass estimates. Fig. 3 presents the histograms of the prior distributions of the lower bounds and upper bounds for the Cases A, B, C, and D including both Monte Carlo sampling of Table 4 distributions and diameter uncertainties.

Results in terms of post-fit residuals and mass estimates are discussed in the following sections.

3 RESULTS

For each Monte Carlo runs, an iterative fit is performed in using the full planetary data sample (see Table 1) and a priori mass values constructed as described in Section 2.2. INPOP19a is the run minimizing the post-fit residuals, among ∼3600 fits.

3.1 The residuals

Fig. 2 shows the MRO/MO distribution of the residuals obtained for the 3600 fits. Furthermore, as indicated by the dot line materializing the INPOP17a rms, more than 70 per cent of the fits have better residuals than INPOP17a. These results show the stability of the method in terms of post-fit residuals and the improvement of INPOP19a with respect to INPOP17a.

3.2 Asteroid masses

Given the prior distributions of lower and upper bounds shown in Fig. 3, fit of masses have been obtained for 343 asteroids over 3600 fits. Only fits with post-fit residuals within the 1σ limit plotted in Fig. 2 are considered, representing 90 per cent of the 3600 Monte Carlo runs. Based on this selection, masses obtained for each of the 343 asteroids have been averaged over the fits, considering only

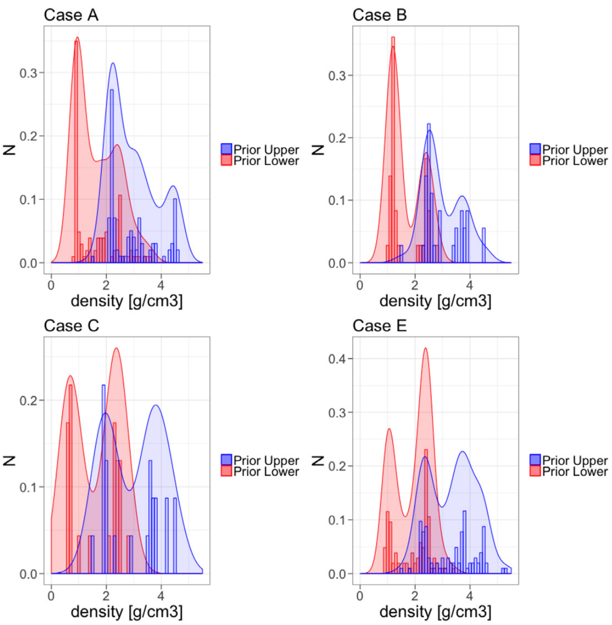

Figure 3. Prior distributions for lower and upper bounds. Are presented here the prior distributions for Cases A, B, C, and E.

estimates significantly different (differences greater than 1σ least-squares uncertainty) from the imposed lower and upper bounds. As discussed in Section 4.2, some asteroids have indeed their fitted masses close to the bounds imposed in the fits. In such cases, the close-to-the-bound estimated values are not taken into account for the estimation of the averaged masses and only asteroids having more than 100 values significantly different from the bounds are considered in this analysis. Uncertainties on the averaged masses correspond to the 1σ dispersion of the averaged distribution of masses. Finally, we kept in our list of estimated masses only the determinations with a ratio of average mass versus the 1σ dispersion greater than 33 per cent. The asteroid masses following the two conditions (σ/M < 33 per cent and having more than 100 values significantly different from the bounds) are given in Table A1 and discussed in the following sections.

3.2.1 *Case A*

The prior distributions of the Case A lower bounds and upper bounds are given in Fig. 3. The posterior distribution of the obtained masses and deduced densities are given in Fig. 4 together with the obtained distribution of the densities according to the diameters. In this case, 103 asteroid masses are estimated with post-fit residuals for the MRO/MO observations of about 1.32 ± 0.32 m. In Table 5, we provide the deduced averaged densities per spectroscopic complex. It is worth noticing that the posterior mean density for the C-type is close to the priors, but it is slightly shifted to higher values (1.70 ± 0.30 g cm^{-3} in comparison to the 1.5 ± 1.0 g cm^{-3} prior distribution). Furthermore, one can also notice the smaller dispersion of the mean density for the C-types in comparison to the one given for the prior. This comment is also true for the X-types and the S-types.

In order to investigate if the departure of the posterior C-complex distribution from its prior is indeed significant, we test the Cases B, C, and D, introducing a shift of the prior distribution towards greater and smaller values (1.8, 1.2, and 2 g cm^{-3}, respectively).

3.2.2 *Cases B, C, and D*

The prior distributions of Cases B, C, and D are given in Fig. 3. The results of Cases B, C, and D have been obtained with 520 runs. In order to compare our results, we performed a supplementary Case A* using the same assumption as in Case A but with 520 runs. Posterior distributions for Cases B, C, and D can be found in Fig. 4 as well as the distributions of the deduced densities versus diameters.

The mean values of the bulk density of the C-complex tend to be higher for Case B compared to Case A*, while the C-complex mean density for Case C (1.73 ± 0.53 g cm^{-3}) is still very close to the values obtained with Case A* (1.65 ± 0.32 g cm^{-3}) and Case B (1.90 ± 0.36 g cm^{-3}) despite its prior distribution. One can also notice the highest uncertainty of the C runs average density C-complex estimate (0.53 g cm^{-3}) to be compared with the A* result (0.32 g cm^{-3}). These results suggest a higher mean density for C-complex compared to the 1.5 g cm^3 initial guess.

Furthermore, the rms for the MRO/MO observations obtained with Case B are significantly better (1.09 ± 0.04 m) than the rms obtained for Case A* (1.25 ± 0.12 m) and Case C (1.28 ± 0.23 m). This last result is also in favour of higher mean bulk density than 1.5 g cm^{-3} for the C-complex.

Finally, according to Fig. 4, the posterior distribution of Case C is shifted in a way that the interval between upper and lower values is reduced (green curves and histograms): lower values are slightly higher and upper values are slightly reduced.

For the other cases, we do not see such a shift of the posterior distribution in comparison to the average of the lower bounds and upper bounds, meaning that the BVLS method tends, as expected, to propose solutions that follow the mean distribution of the bounds.

As one can see in Table 5, the rms of the Mars post-fit residuals obtained with Case D has a greater dispersion (0.42 m) than the one obtained with Case B (0.04 m). Furthermore, the posterior Case D distribution of densities shows a small departure towards smaller values in comparison to its prior distribution.

In conclusion, Case B indicates a more favourable value for the C-complex density of about 1.8 g cm^{-3} than a value of 2.0 g cm^{-3} (Case D) or a value of 1.5 g cm^{-3} (Case A*). The worst results were obtained with Case C.

3.2.3 *Case E*

Combining the four previous cases, Case E gives a general overview of the results obtained with 3 617 runs. In this configuration with estimations of masses obtained with enlarged priors (considering Cases A, B, C, and D together), we increase the dispersion of the mass distribution and consequently the σ/M ratio. This is a reason why we obtained about the same number of estimated masses (103 for Case E versus 102 for Case A), although the number of runs was two times higher for Case E compared to Case A (3617 versus 1684). Furthermore, the rms for the MO/MRO observations of Case E has a dispersion two times larger than in Case A (0.66 versus 0.32 m), although we have twice the number of runs for Case A.

If one does not include Case D in the combination (Case E*), we obtain rms of about (1.26 ± 0.26 m), far more compatible with the other rms dispersions. For Case E*, only 97 asteroid masses are then estimated and the dispersion of the estimated complex densities is slightly higher than for Case E. For Case E, the posterior distribution of the densities can be found in Fig. 5 and the distribution of the densities regarding the diameters in presented in Fig. 5. Case E distribution of the obtained masses (Fig. 5) differs from the one

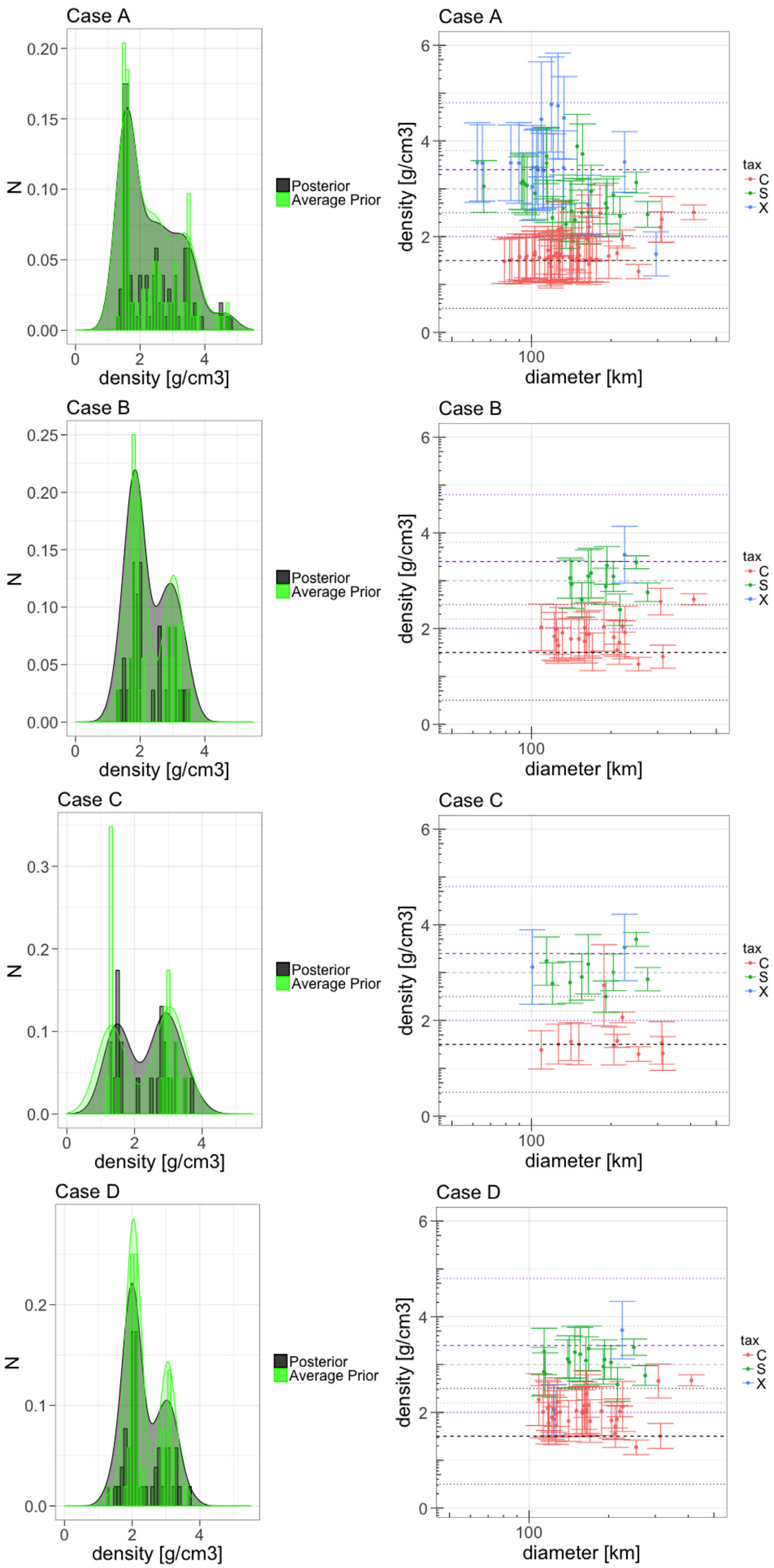

Figure 4. Posterior distributions of Cases A, B, C, and D (left-hand side). Distribution of estimated densities (in log scale) relative to diameters for Cases A, B, C, and D (right-hand side).

Table 5. Results obtained for each studied case. The first row gives the number of fits operated for each case. The second row gives the statistics of the post-fit residuals for the MRO and MO data. Third row indicates how many masses have been retained after the filtering explained in Section 3.2. Rows 4–6 give the averaged values of densities in g cm^{-3} estimated for each spectral complex. The last row indicates the repartitions of the asteroids per classes.

	A	B	A*	C	D	E	E*
Number of runs	1900	600	600	600	600	3700	3100
(O-C) MRO rms (m)	1.32 ± 0.32	1.09 ± 0.04	1.25 ± 0.12	1.28 ± 0.23	1.14 ± 0.43	1.39 ± 0.66	1.27 ± 0.26
Number of filtered masses	102	35	32	22	51	103	96
C-complex	1.70 ± 0.31	1.90 ± 0.36	1.65 ± 0.32	1.73 ± 0.53	2.02 ± 0.31	1.80 ± 0.30	1.74 ± 0.31
S-complex	2.89 ± 0.46	2.99 ± 0.30	2.94 ± 0.20	3.01 ± 0.36	3.05 ± 0.22	2.98 ± 0.29	2.99 ± 0.31
X-complex	3.55 ± 0.72	3.54	3.57	3.32 ± 0.29	2.89 ± 1.18	3.53 ± 0.36	3.61 ± 0.42
C, S, X repartition	56 per cent, 25 per cent, 19 per cent	67 per cent, 30 per cent, 3 per cent		52 per cent, 39 per cent, 9 per cent	67 per cent, 29 per cent, 4 per cent	40 per cent, 40 per cent, 20 per cent	44 per cent, 39 per cent, 17 per cent

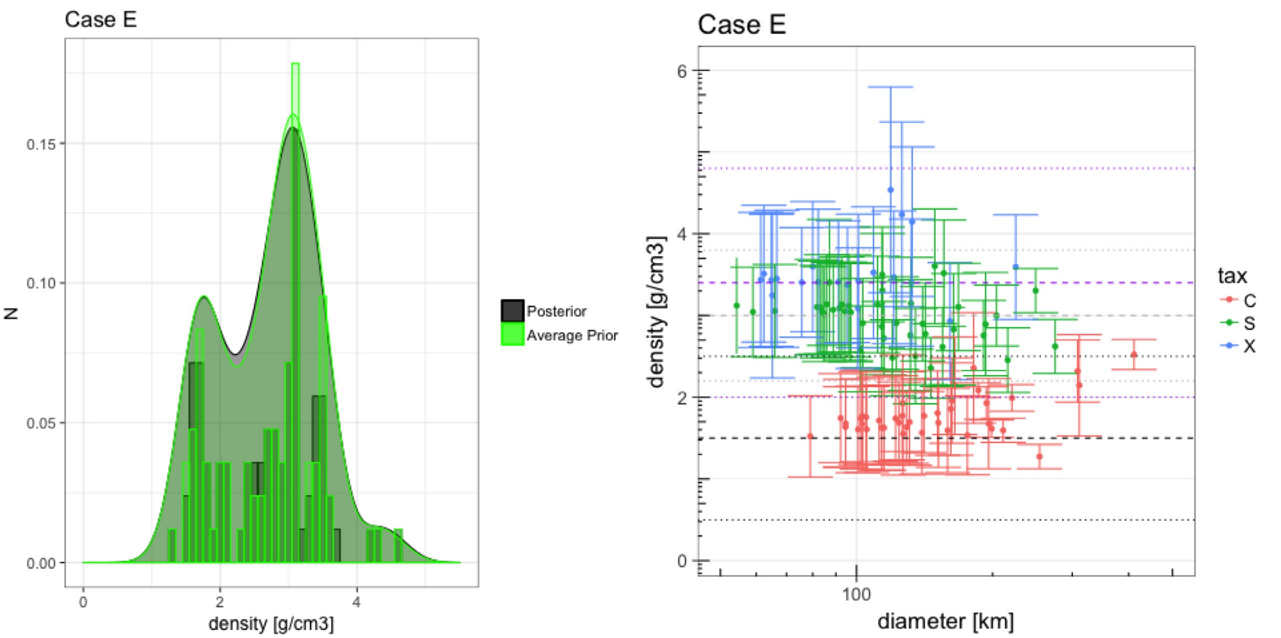

Figure 5. Posterior distributions of Case E (left-hand side). Distribution of estimated densities (in log scale) relative to diameters for Case E (right-hand side). The uncertainties correspond to 1σ dispersion.

obtained with Case A (Fig. 4). Although for Case A about 10 per cent of the C-complex asteroids with estimated masses have diameters smaller than 100 km, only 1C-complex asteroid for Case E has a diameter smaller than 100 km. This can be explained by a reduced dispersion of the fitted masses with Case A compared to Case E, especially for smaller perturbers.

Finally, one can see that for Case A, it is possible to have an X-complex object with a density smaller than 2 g cm^{-3} while for Case E, 99.98 per cent (3σ) of the X-complex asteroids have their densities greater than 2.35 g cm^{-3}. We recall that the prior for the X-complex is the same for all Cases. As already noticed, Case E densities follow closely the distribution of the mean between the lower and the upper bounds imposed to the fit.

4 DISCUSSION

4.1 Source of uncertainties

The estimations of asteroid masses with planetary ephemerides depend mainly on the impact of the body on the planetary distances affected by their perturbations. As the Mars orbiters provide the most accurate observed distances over more than 40 yr for a planet that, by its close proximity to the Main Belt, is the most affected by asteroid perturbation, it is clear that the impact of the asteroids on the Mars–Earth distances is an efficient criterion for characterizing the accuracy of the asteroid mass determination (Kuchynka et al. 2010). An asteroid having an important impact on the Earth–Mars distances will be more easily characterized (Kuchynka et al. 2010; Kuchynka & Folkner 2013).

In Fig. 6, we present masses obtained with Case E considering the impact of the asteroid on the Earth–Mars distances, the mass dispersion and the asteroid complexes. The most accurate determinations (with dispersion 15 per cent smaller than the fitted masses) were obtained for asteroids inducing perturbations larger than 10 m (dashed line).

The comparison between the results of Cases A and E indicates that Case A determinations are less accurate than those obtained with Case E, especially for objects inducing less than 10-m perturbations. One can also note that for the same population of objects (inducing less than 10-m perturbation), Case A provides

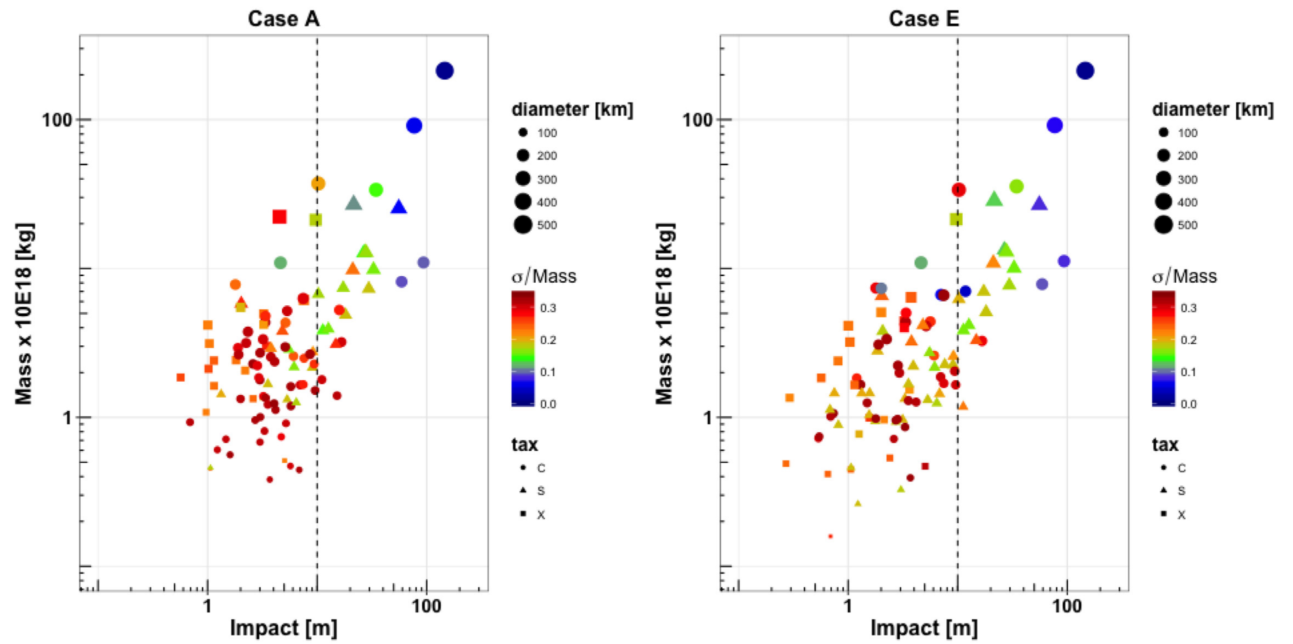

Figure 6. Distribution of the estimated masses according to their impact on the Earth–Mars distances over 40 yr. The σ/mass ratio gives the ratio between the mass dispersion over the average mass.

more mass estimates for the C-complex asteroids than for Case E where the sampling of fitted masses is more diverse in terms of complexes. This can also be illustrated by the number of low perturbers (inducing less than 1-m perturbations) in Cases A (2) and E (11).

Finally, we noticed that for Case A, only two masses inducing less than 1-m perturbations are estimated with an accuracy better than 33 per cent, while for Case E, about 10 low perturber masses are obtained.

4.2 Case of limited estimates

As explained previously during the fits, it happens that some masses are estimated with values very close or equal to the bounds imposed to the fit. In such cases, the close to the bound values are not included in the computation of the average masses, leading to a smaller numbers of runs used for the average mass determinations.

In Fig. 7, we show the histograms of the numbers of runs used for estimating masses inducing more than 5-m perturbations (black) and for those inducing less than 1-m perturbations (red). It appears that 97 per cent of the asteroids inducing more than 5-m dispersion on the Earth–Mars distances have their masses averaged over more than 100 runs, while, on the opposite, 85 per cent of the asteroids inducing less than 1-m dispersion have their masses estimated with less than 100 runs.

In conclusion, the fact that masses can stay close to the lower bounds or the upper bounds of the fit can be considered as an indication that these masses do not produce enough perturbations to be individualized in the fit. These masses are not seen as reliable estimations, but they are part of the fit. Because of the correlations between parameters, these unreliable estimates impact directly the least-squares uncertainties. The least-squares errors (LS σ) are more important for masses correlated with badly fitted masses, while, in

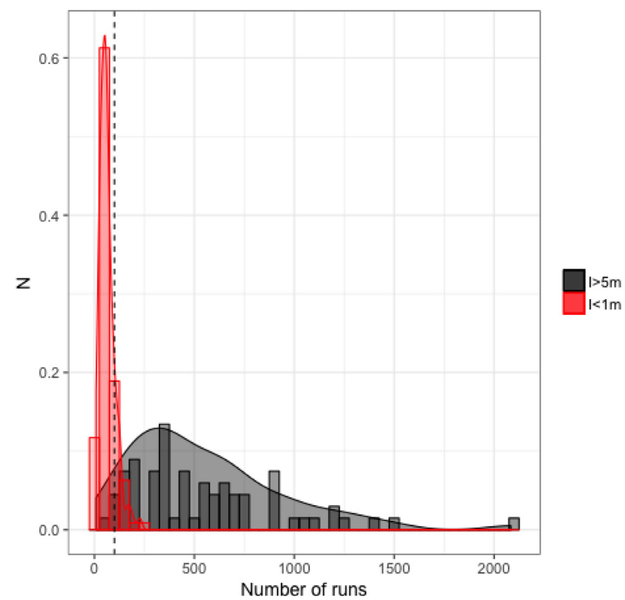

Figure 7. Histogram of the number of runs used for computing averaged masses for masses inducing more than 5 m perturbations and masses inducing less than 1 m.

the contrary, a small least-squares error indicates an estimation less sensitive to these unreliable determinations. In Table A1, we give the least-squares errors (columns 9 and 12) that can be compared with the dispersion obtained with the Mont Carlo simulations (MC σ, columns 10 and 13). If one considers the ratio between the LS σ and the estimated masses, only 41 asteroids have their masses estimated with an accuracy better than 33 per cent. These objects are indicated with a star in Table A1.

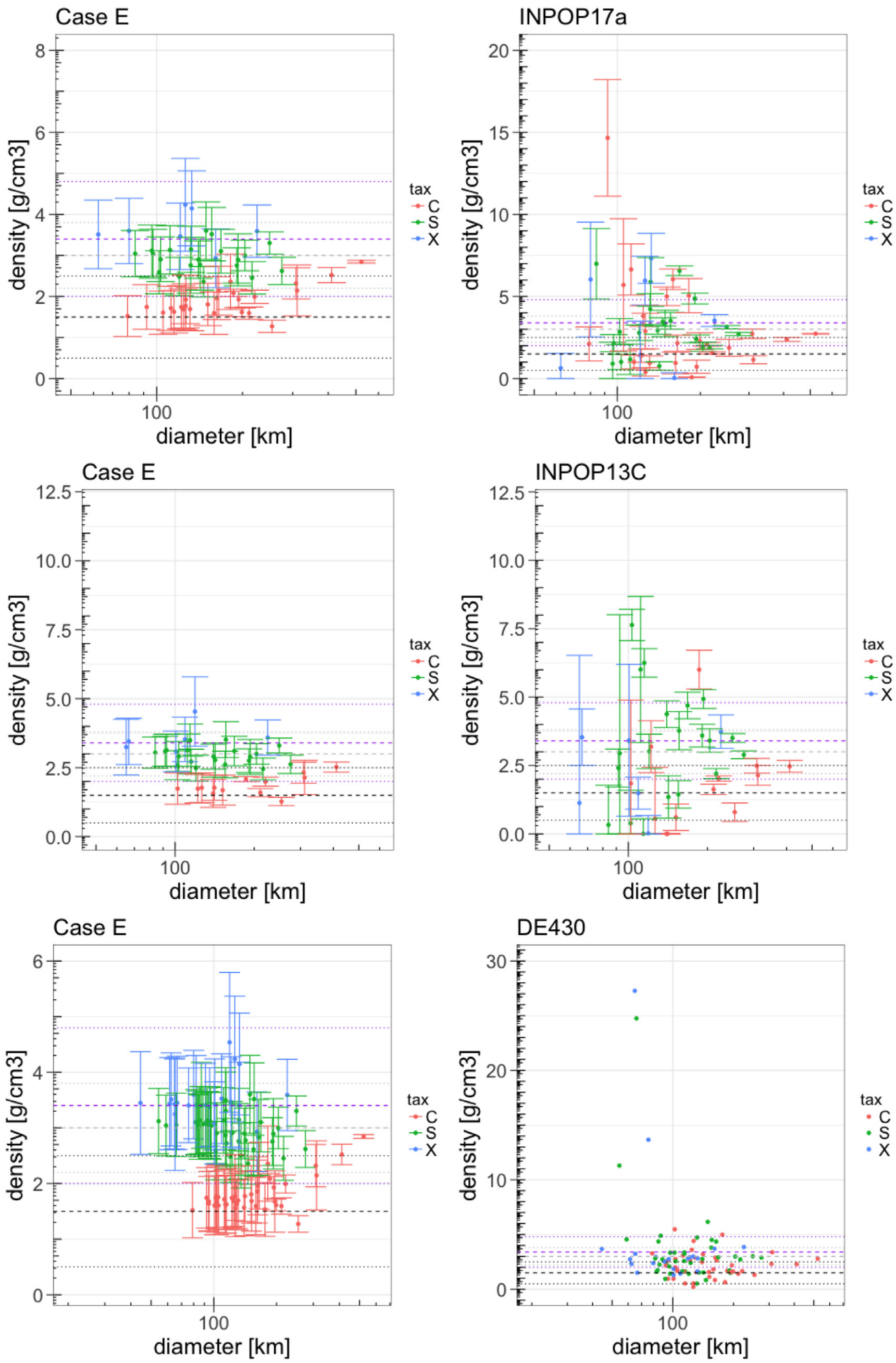

Figure 8. Comparisons between Case E, INPOP17a, INPOP13c, and DE430. 54 asteroids have common values between Case D and INPOP17a while 42 common values are found between Case D and INPOP13c (see Table 6 for complete comparisons).

4.3 Comparisons

4.3.1 Comparison with previous planetary ephemeride mass determinations

In Fig. 8, we show the densities deduced from asteroid mass determinations obtained with INPOP17a, INPOP13c, DE430, and Case E. As one can see, the dispersion and uncertainties of INPOP13c and INPOP17a densities are quite large. More importantly, as we show in Table 6, gathering statistics for asteroids having their masses both estimated with INPOP17a and Case E on one hand, and INPOP13c and Case E on the other hand, the averaged complex densities are far from the expected values, leading to unrealistic mass and density estimates for the previous INPOP versions. The results obtained in this work represent an important improvement in comparison to the previous INPOP asteroid mass estimations.

Table 6. Averaged complex densities for INPOP17a, INPOP13c, DE430, and Case E. The row starting with Case E indicates the averaged complex densities obtained in Case E for the same objects as INPOP17a, INPOP13c, and DE430.

		C-complex ($\mathrm{g\,cm^{-3}}$)	S-class ($\mathrm{g\,cm^{-3}}$)	M-class ($\mathrm{g\,cm^{-3}}$)
INPOP17a	54	3.05 ± 3.03	3.16 ± 1.86	3.56 ± 2.93
Case E @ INPOP17a		1.89 ± 0.35	2.96 ± 0.33	3.64 ± 0.44
INPOP13c	42	1.83 ± 1.61	3.44 ± 2.02	2.22 ± 1.55
Case E @ INPOP13c		1.86 ± 0.34	2.96 ± 0.30	3.57 ± 0.51
DE430	103	2.17 ± 1.17	3.47 ± 3.97	4.29 ± 5.83
Case E @ DE430		1.80 ± 0.3	2.99 ± 0.28	3.52 ± 0.36

Finally, in Fig. 8, we also show density estimates deduced from masses provided by DE430 and densities for the same objects obtained in Case E. Clearly, some of the DE430 densities are largely inconsistent with their corresponding spectral types or are even unrealistic ($>$10 $\mathrm{g\,cm^{-3}}$). This could be due to differences in the diameter values used for the computation of DE430 a priori values.

In any case, our new estimations improve the dispersion of the densities by more than a factor of 10 for the S- and X-complexes (Table 6).

Finally, we compare our estimates with the 27 masses proposed by Kuchynka & Folkner (2013) as being reliable considering systematic errors induced by the asteroid selection procedure. The masses obtained with Case E and by Kuchynka & Folkner (2013) are presented in Table 7. Most of the estimations are consistent at 2σ. The biggest differences between our estimates and the one deduced from Kuchynka & Folkner (2013) correspond to high systematic errors estimated by Tikhonov regularization, e.g. (10) Hygiea, (704) Interamnia, or (511) Davida. Furthermore, for the two biggest differences (Pallas and Hygiea), it is interesting to note that the comparisons between masses obtained by Kuchynka & Folkner (2013) and Folkner et al. (2014) give differences compatible with 3σ uncertainties proposed by Kuchynka & Folkner (2013, see Table 7). The Folkner et al. (2014) DE430 masses were obtained after an update of the data sample (addition of more recent observations of Mars positions) in using the same selection of asteroid to be estimated. The differences between the two JPL estimates provide additional information about the uncertainties, leading once again to consistent results with our work.

4.3.2 Comparisons with masses published in Carry (2012)

In Carry (2012), asteroid masses were obtained by compiling values obtained by different methods: from s/c fly-bys, binary systems for the direct measurements, but also from planetary ephemerides (like in this paper) and asteroid close-encounters for the indirect methods. Statistics of masses deduced from diameter measurements and densities hypotheses are also discussed. Considering masses deduced from planetary ephemerides determinations, Carry (2012) averaged the masses obtained by different teams (Pitjeva 2010; Fienga et al. 2012; Folkner et al. 2014) by computing a weighted mean, the weights corresponding to the published uncertainties.

As for DE430 determinations, there is no published uncertainties, Carry (2012) had used 10 per cent as weights for the DE430 contribution to the estimation of the average planetary ephemerides values.

Based on this work and Kuchynka & Folkner (2013), it appears that 10 per cent uncertainty is clearly underestimating the DE430 uncertainty. In Kuchynka & Folkner (2013), only 27 asteroids over 343 have been estimated with uncertainties smaller than 33 per cent of the corresponding masses. Carry (2012) values for planetary ephemerides masses are then, by construction, biased towards DE430 values as the published uncertainties of the other planetary ephemerides masses are larger than 10 per cent. However, despite this comment, we have compared masses commonly published by

Table 7. Reliable masses obtained by Kuchynka & Folkner (2013) labelled as KF and their corresponding values determined with Case E. The uncertainties are given at 1σ. The KF last column gives the information about the systematic error obtained by Tikhonov regularization in Kuchynka & Folkner (2013). The last column gives mass values extracted from Folkner et al. (2014).

IAU designation Number	Diameters (km)	Mass Case E ($\times10^{18}$ kg)	1σ ($\times10^{18}$ kg)	Mass KF ($\times10^{18}$ kg)	1σ KF ($\times10^{18}$ kg)	KF systematic error ($\times10^{18}$ kg)	DE430 mass ($\times10^{18}$ kg)
1	946.0	938.668	2.6	940.623	5.694	2.697	941.295
4	525.4	259.117	0.7	259.503	1.648	0.450	259.087
2	523.000	213.176	5.134	202.268	4.195	1.199	208.657
324	220.690	11.207	0.915	10.188	0.749	0.449	9.333
10	411.000	91.672	6.697	105.030	8.390	2.547	83.061
19	211.000	7.842	0.724	7.791	0.899	0.300	6.961
3	249.000	26.702	2.185	26.819	1.648	1.348	24.314
704	308.300	35.592	5.837	39.405	6.892	4.795	35.328
532	191.000	10.051	1.567	12.885	2.697	1.199	6.261
9	168.000	7.703	1.326	6.892	1.348	0.449	7.244
7	216.000	12.943	2.085	14.833	1.648	0.599	14.359
29	204.000	13.333	1.660	10.338	2.397	1.498	13.280
15	275.000	28.541	3.604	26.070	2.847	0.749	31.444
6	193.000	10.889	2.383	8.390	1.948	0.899	5.587
14	155.000	5.097	0.941	6.592	1.348	0.300	7.397
8	140.000	4.165	0.654	4.345	0.749	0.300	3.961
18	146.000	3.842	0.604	4.045	1.049	0.449	1.350
511	311.000	33.791	9.773	29.516	8.390	6.892	34.938
16	225.000	21.422	3.819	17.680	4.195	1.348	22.930
23	120.000	2.246	0.421	1.648	0.599	0.150	1.274
42	102.000	1.440	0.292	1.498	0.449	0.150	1.859

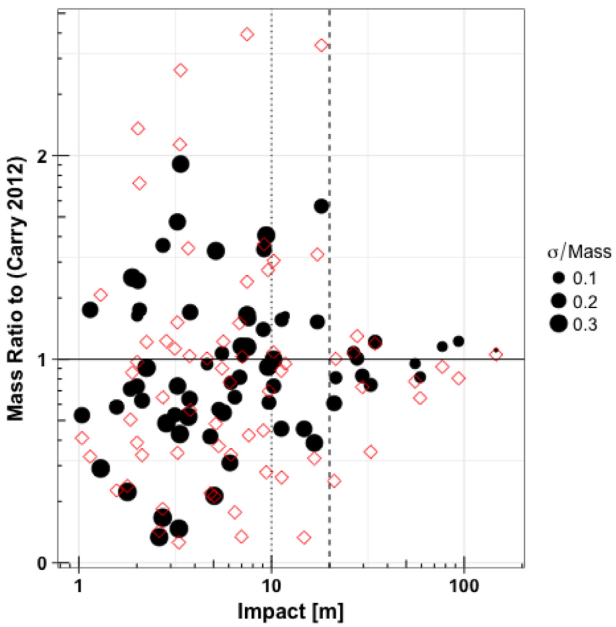

Figure 9. Distribution of the ratios Case E masses over Carry (2012) masses (dots) and DE430 masses over Carry (2012) masses (square) relative to the impact of the asteroids on the Earth–Mars distances. The size of the dots indicates the σ/Mass ratio of the Case E masses. The vertical lines indicate the limit for perturbations equal to 20 km (dashed line) and 10 km (dot line).

Carry (2012), DE430, and Case E. We have found 36 masses common to the three studies. As one can see in Fig. 9, the ratio between masses obtained by Carry (2012) and Case E are closer to 1 than the ratio between Carry (2012) masses and DE430 masses, especially for objects inducing less than 20 m. This shows that Case E masses are consistent with the weighted averaged masses obtained with previous estimates.

4.3.3 Comparisons with binary systems and spacecraft fly-bys

In Table 3, we compare masses obtained with Case E and values deduced from the observations of the asteroid satellite or from the navigation tracking of a spacecraft orbiting an asteroid. These two methods are the most accurate procedures for measuring the asteroid masses. Their uncertainties are usually small, thus are good candidates for comparison purposes. Our estimates from Case E are consistent at 1σ level to those based on the spacecraft or satellite data (Table 3).

NASA's future space mission Psyche is considered a remnant core of a differentiated object. Older mass estimates, combined with the most up-to-date diameter measurement (Hanuš et al. 2017; Shepard et al. 2017), gave a relatively high density of 4.5 g cm^{-3}. However, newer estimation of the density, as in Avdellidou, Delbo' & Fienga (2018), Viikinkoski et al. (2018), and in this work, results in a lower value that does not indicate the presence of a metallic core.

5 CONCLUSIONS

In this work, we present a new method for a better control of the asteroid mass determination in planetary ephemerides. We show that by randomly selecting constraints in the least-squares procedure we were able to find masses and then densities consistent with the known complexes of the asteroids. Moreover, our fits have very good residuals (with rms below 1.2m) for Mars orbiters. In comparison to previous mass estimates obtained by planetary ephemerides, we found that our new mass determinations lead to more consistent determinations of the bulk densities for the main spectroscopic complexes.

ACKNOWLEDGEMENTS

This work was supported by the French Agence National de la Recherche (ANR) ORIGINS (ANR-PRC-18TBD). The authors thank Marco Delbo for his precious help. CA was supported by the French National Research Agency under the project 'Investissements d'Avenir' UCA^{JEDI} with the reference number ANR-15-IDEX-01. The authors also thank Benoit Carry for his help and comments during the writing of the manuscript. This work is based on data provided by the Minor Planet Physical Properties Catalogue (MP3C) of the Observatoire de la Cote d'Azur (https://mp3c.oca.eu/). The work of JH has been supported by the Czech Science Foundation through grant 18-09470S and by the Charles University Research programme no. UNCE/SCI/023. The authors thank M. Granvik for his very constructive comments.

REFERENCES

Abe S. et al., 2006, Science, 312, 1344
Alí-Lagoa V., Müller T. G., Usui F., Hasegawa S., 2018, A&A, 612, A85
Avdellidou C., Delbo' M., Fienga A., 2018, MNRAS, 475, 3419
Barnouin O. S. et al., 2019, Nature Geosci., 12, 247
Belton M. J. S. et al., 1995, Nature, 374, 785
Binzel R. P. et al., 2019, Icarus, 324, 41
Bottke W. F. J., Vokrouhlický D., Rubincam D. P., Nesvorný D., 2006, Ann. Rev. Earth Planet. Sci., 34, 157
Bus S. J., Binzel R. P., 2002, Icarus, 158, 146
Carry B., 2012, P&SS, 73, 98
Carry B. et al., 2019, A&A, 623, A132
Carvano J. M., Hasselmann P. H., Lazzaro D., Mothé-Diniz T., 2010, A&A, 510, A43
Chesley S. R. et al., 2003, Science, 302, 1739
Chesley S. R. et al., 2014, Icarus, 235, 5
Consolmagno G., Britt D., Macke R., 2008, Chemie der Erde/Geochem., 68, 1
DeMeo F. E., Carry B., 2013, Icarus, 226, 723
DeMeo F. E., Binzel R. P., Slivan S. M., Bus S. J., 2009, Icarus, 202, 160
Descamps P. et al., 2007, Icarus, 187, 482
Descamps P. et al., 2008, Icarus, 196, 578
Descamps P. et al., 2011, Icarus, 211, 1022
Fang J., Margot J.-L., Rojo P., 2012, AJ, 144, 70
Fienga A., Manche H., Laskar J., Gastineau M., 2008, A&A, 477, 315
Fienga A. et al., 2009, A&A, 507, 1675
Fienga A., Laskar J., Manche H., Kuchynka P., Desvignes G., Gastineau M., Cognard I., Thereau G., 2011, Celest. Mech. Dyn. Astron., 111, 363
Fienga A., Laskar J., Manche H., Gastineau M., Verma A., 2012, DPAC INPOP Final Release: INPOP10e, Notes Scientifiques et Techniques de l'Institut de mécanique céleste
Fienga A., Laskar J., Manche H., Gastineau M., Verma A., 2014, New INPOP Release: INPOP13c, preprint (arXiv:1405.0484)
Fienga A., Laskar J., Manche H., Gastineau M., Verma A., 2016, Tests of GR with INPOP15a Planetary Ephemerides: Estimations of Possible Supplementary Advances of Perihelia for Mercury and Saturn, preprint (arXiv:1601.00947)

Folkner W. M., Williams J. G., Boggs D. H., Park R. S., Kuchynka P., 2014, Int. Netw. Prog. Rep., 196, C1
Fujiwara A. et al., 2006, Science, 312, 1330
Gaia Collaboration et al., 2018, A&A, 616, A13
Hanuš J. et al., 2017, A&A, 601, A114
Hanuš J., Delbo M., Durech J., Alí-Lagoa V., 2015, Icarus, 256, 101
Hanuš J., Marchis F., Viikinkoski M., Yang B., Kaasalainen M., 2017a, A&A, 599, A36
Hanuš J. et al., 2017b, A&A, 601, A114
Hanuš J. et al., 2018, A&A, 620, L8
Harris A. W., 2006, in Lazzaro D., Ferraz-Mello S., Fernandez J. A., eds, Proc. IAU Symp. 229, Asteroids, Comets, Meteors, Cambridge University Press, cambridge
Harris A. W., Lagerros J. S. V., 2002, in Bottke W. F.,, Jr, Cellino A., Paolicchi P., Binzel R. P., eds, Asteroids III. Univ. Arizona Press, Tucson, p. 205
Kuchynka P., 2010, PhD thesis, Observatoire de Paris, France
Kuchynka P., Folkner W. M., 2013, Icarus, 222, 243
Kuchynka P., Laskar J., Fienga A., Manche H., 2010, A&A, 514, A96
Lawson C., Hanson R., 1974, Solving Least Squares Problems. Society for Industrial and Applied Mathematics, New Jersey
Lawson C., Hanson R., 1995, Solving Least Squares Problems: New edition. Society for Industrial and Applied Mathematics, New Jersey
Lazzaro D., Angeli C. A., Carvano J. M., Mothé-Diniz T., Duffard R., Florczak M., 2004, Icarus, 172, 179
Mainzer A., Usui F., Trilling D. E., 2015, in Michel P. et al., eds, Asteroids IV. Univ. Arizona Press, Tucson, p. 89
Marchis F., Hestroffer D., Descamps P., Berthier J., Laver C., de Pater I., 2005a, Icarus, 178, 450
Marchis F., Descamps P., Hestroffer D., Berthier J., 2005b, Nature, 436, 822
Marchis F., Descamps P., Berthier J., Hestroffer D., Vachier F., Baek M., Harris A. W., Nesvorný D., 2008a, Icarus, 195, 295
Marchis F., Descamps P., Baek M., Harris A. W., Kaasalainen M., Berthier J., Hestroffer D., Vachier F., 2008b, Icarus, 196, 97
Masiero J. R. et al., 2011, ApJ, 741, 68
Masiero J. R., Mainzer A. K., Grav T., Bauer J. M., Cutri R. M., Nugent C., Cabrera M. S., 2012, ApJ, 759, L8
Masiero J. R., Grav T., Mainzer A. K., Nugent C. R., Bauer J. M., Stevenson R., Sonnett S., 2014, ApJ, 791, 121
Mouret S., Hestroffer D., Mignard F., 2007, A&A, 472, 1017
Mouret S., Hestroffer D., Mignard F., 2008, Planet. Space Sci., 56, 1819
Moyer T., 1971, IOM 3215-37, DPODP Manual. JPL, Jet Propulsion Laboratory, Pasadena
Pätzold M. et al., 2011, Science, 334, 491
Pitjeva E. V., 2010, in Klioner S. A., Seidelmann P. K., Soffel M. H., eds, Relativity in Fundamental Astronomy , Proc. IAU Symp. 261. Cambridge Univ. Press, Cambridge, p. 170
Popescu M., Licandro J., Carvano J. M., Stoicescu R., de León J., Morate D., Boacă I. L., Cristescu C. P., 2018, A&A, 617, A12
Rojo P., Margot J. L., 2011, ApJ, 727, 69
Rozitis B., Green S. F., 2014, A&A, 568, A43
Rozitis B., MacLennan E., Emery J. P., 2014, Nature, 512, 174
Russell C. T. et al., 2012, Science, 336, 684
Russell C. T. et al., 2016, Science, 353, 1008
Scheeres D. J. et al., 2019, Nature Astron., 3, 352
Shepard M. K. et al., 2017, Icarus, 281, 388
Siltala L., Granvik M., 2017, Icarus, 297, 149
Siltala L., Granvik M., 2019, preprint (arXiv:1911.05418)
Somenzi L., Fienga A., Laskar J., Kuchynka P., 2010, Planet. Space Sci., 58, 858
Standish E. M., Hellings R. W., 1989, Icarus, 80, 326
Stark P. B., Parker R. L., 1995, Comput. Stat., 10, 129
Tholen D. J., 1989, Asteroid II , Asteroid Taxonomic Classifications, University of Arizona Press, Tucson, p. 1139
Tyler G. L., Brenkle J. P., Komarek T. A., Zygielbaum A. I., 1977, J. Geophys. Res., 82, 4335
Usui F. et al., 2011, PASJ, 63, 1117
Viikinkoski M., Hanuš J., Kaasalainen M., Marchis F., Ďurech J., 2017, A&A, 607, A117
Viikinkoski M. et al., 2018, A&A, 619, L3
Viswanathan V., Fienga A., Gastineau M., Laskar J., 2017, Notes Scientifiques et Techniques de l'Institut de Mecanique Celeste, Institut de mécanique céleste, Paris, p. 108
Viswanathan V., Fienga A., Minazzoli O., Bernus L., Laskar J., Gastineau M., 2018, MNRAS, 476, 1877
Vokrouhlický D., Bottke W. F., Chesley S. R., Scheeres D. J., Statler T. S., 2015, in Michel P. et al., eds, Asteroids IV. Univ. Arizona Press, Tucson, p. 509
Watanabe S. et al., 2019, Science, 364, 268
Williams J. G., 1984, Icarus, 57, 1
Xu S., Binzel R. P., Burbine T. H., Bus S. J., 1995, Icarus, 115, 1
Yang B., Wahhaj Z., Beauvalet L., Marchis F., Dumas C., Marsset M., Nielsen E. L., Vachier F., 2016, ApJ, 820
Yeomans D. K. et al., 1997, Science, 278, 2106
Yeomans D. K. et al., 2000, Science, 289, 2085

SUPPORTING INFORMATION

Supplementary data are available at *MNRAS* online.

Table A1. Asteroid masses (M) and densities (ρ) derived in this work.

Please note: Oxford University Press is not responsible for the content or functionality of any supporting materials supplied by the authors. Any queries (other than missing material) should be directed to the corresponding author for the article.

APPENDIX: SUPPLEMENTARY MATERIAL AVAILABLE ONLINE

See Table A1.

Table A1. Asteroid masses (M) and densities (ρ) derived in this work. The column p_V gives the value of the geometric visible albedo. The column $\mathrm{Ref_S}$ gives the reference publication of the adopted spectral class, whenever this is available; the reference number is the following: 1 = DeMeo et al. (2009), 2 = Bus & Binzel (2002), 3 = Lazzaro et al. (2004), 4 = Tholen (1989), and 5 = Xu et al. (1995). The column D reports the adopted asteroid diameter and the column $\mathrm{Ref_D}$ the corresponding reference according to the following scheme: a = Usui et al. (2011), b = Masiero et al. (2011), c = Masiero et al. (2014), d = Hanuš et al. (2017b), e = Viikinkoski et al. (2017), f = Russell et al. (2012), g = Pätzold et al. (2011), h = Hanuš et al. (2017a), and i = Russell et al. (2016). The last column corresponds to the perturbation on the Earth–Mars distance over an interval of 40 yr. Two type of uncertainties are given: one labelled LS derived directly from the least-squares fits, and one labelled MC corresponding to the dispersion of the estimations over 3 600 runs. Finally, the star indicates masses estimated with LS σ 33 per cent smaller than the fitted masses. The full table is available online only.

Asteroid	p_V	T	$\mathrm{Ref_S}$	D (m)	σ (km)	$\mathrm{Ref_D}$	M $\times 10^{18}$ (kg)	LS σ_M $\times 10^{18}$ (kg)	MC σ_M $\times 10^{18}$ (kg)	ρ (g cm^{-3})	LS σ_ρ (g cm^{-3})	MC σ_ρ (g cm^{-3})	Impact (m)	Complex
1	0.087	C	1	946	3	i	938.668	2.309	7e−3	2.118	5e−3	1.6e−5	793.741	C
2*	0.142	B	1	523	10	d	213.196	1.415	5.134	2.846	0.019	0.068	146.27	C
3*	0.246	Sq	1	249	5	e	26.702	0.885	2.185	3.303	0.109	0.27	55.639	S
4	0.342	V	1	525.4	0.1	f	259.117	0.667	3e−4	3.412	9e−3	1e−04	1198.953	V
5*	0.27	S	1	114	4	j	2.716	0.326	0.45	3.501	0.420	0.581	5.533	S
6*	0.24	S	2	193	6	e	10.889	0.903	2.383	2.893	0.240	0.633	21.15	S
7*	0.179	S	1	216	7	d	12.943	0.632	2.085	2.453	0.120	0.395	27.822	S
8*	0.23	Sw	1	140	4	d	4.165	0.426	0.654	2.899	0.297	0.455	12.664	S
9*	0.16	T	3	168	3	d	7.703	0.949	1.326	3.103	0.382	0.534	29.606	S
10*	0.058	C	1	411	20	d	91.672	3.444	6.697	2.522	0.095	0.184	77.003	C
11*	0.19	Sq	1	156	5	d	6.992	1.130	1.294	3.517	0.569	0.651	17.301	S
15*	0.25	S	1	275	5	e	28.541	1.532	3.604	2.621	0.141	0.331	21.555	S
16*	0.181	Xk	1	225	4	d	21.422	2.508	3.819	3.592	0.421	0.64	9.701	X

This paper has been typeset from a TEX/LATEX file prepared by the author.